frontiers | Frontiers in Materials

TYPE Original Research
PUBLISHED 06 February 2023
DOI 10.3389/fmats.2023.1142237

OPEN ACCESS

EDITED BY
Kequan Yu,
Tongji University, China

REVIEWED BY
Xiangyi Zhu,
Changsha University of Science and Technology, China
Haoliang Wu,
Sun Yat-sen University, China

*CORRESPONDENCE
Bo-Tao Huang,
botaohuang@zju.edu.cn
Jian-Guo Dai,
cejgdai@polyu.edu.hk

SPECIALTY SECTION
This article was submitted to Structural Materials,
a section of the journal
Frontiers in Materials

RECEIVED 11 January 2023
ACCEPTED 24 January 2023
PUBLISHED 06 February 2023

CITATION
Lao J-C, Xu L-Y, Huang B-T, Zhu J-X, Khan M and Dai J-G (2023), Utilization of sodium carbonate activator in strain-hardening ultra-high-performance geopolymer concrete (SH-UHPGC). *Front. Mater.* 10:1142237.
doi: 10.3389/fmats.2023.1142237

Utilization of sodium carbonate activator in strain-hardening ultra-high-performance geopolymer concrete (SH-UHPGC)

Jian-Cong Lao[1], Ling-Yu Xu[1], Bo-Tao Huang[1,2]*, Ji-Xiang Zhu[1], Mehran Khan[1] and Jian-Guo Dai[1]*

[1]Department of Civil and Environmental Engineering, The Hong Kong Polytechnic University, Hong Kong, China, [2]Institute of Advanced Engineering Structures, Zhejiang University, Hangzhou, China

In this study, strain-hardening ultra-high-performance geopolymer concrete (SH-UHPGC) was produced using Na_2CO_3, Na_2SiO_3 and their hybridization (1:1 in mole ratio) as alkaline activators. An ultra-high compressive strength was achieved for all the developed strain-hardening ultra-high-performance geopolymer concrete (i.e., over 130 MPa). Strain-hardening ultra-high-performance geopolymer concrete with hybrid Na_2CO_3 and Na_2SiO_3 activators showed the highest compressive strength (186.0 MPa), tensile strain capacity (0.44%), and tensile strength (11.9 MPa). It should be highlighted that very significant multiple cracking can be observed for all the strain-hardening ultra-high-performance geopolymer concrete even at a very low tensile strain level (e.g., 0.1%). According to the reaction heat, microstructures, and chemical composition analyses, strain-hardening ultra-high-performance geopolymer concrete with hybrid activators had the highest reaction degree, while that of Na_2CO_3-based strain-hardening ultra-high-performance geopolymer concrete was the lowest. It was found that the Na_2CO_3-based strain-hardening ultra-high-performance geopolymer concrete showed the best sustainability, and the strain-hardening ultra-high-performance geopolymer concrete with hybrid Na_2SiO_3 and Na_2CO_3 presented the best overall performance (considering the mechanical performance, energy consumption, environmental impact, and economical potential). The findings of this work provide useful knowledge for improving the sustainability and economic potential of strain-hardening ultra-high-performance geopolymer concrete materials.

KEYWORDS

Ultra-High-Performance Concrete (UHPC), Strain-Hardening Geopolymer Composites (SHGC), Strain-Hardening Cementitious Composites (SHCC), alkali-activated fly ash/slag, fiber-reinforced geopolymer composites, multiple cracking, low carbon

1 Introduction

In the past few decades, breakthroughs have been achieved in both strength and ductility improvements of concrete materials, leading to the generation of ultra-high-performance concrete (UHPC) (Xiang et al., 2017; Huang et al., 2021a; Yoo et al., 2022a; Khan et al., 2022) and Engineered/Strain-Hardening Cementitious Composites (ECC/SHCC) (Li, 2019; Wu et al., 2021a; Wu et al., 2021b; Deng et al., 2023). Specifically, UHPC is an innovative material with densely-packed matrix, which typically presents an ultra-high compressive strength (e.g., over 120 MPa), excellent durability and high toughness (Yoo et al., 2016; Huang et al., 2022a; Jang et al., 2022). However, in order to achieve ultra-high strength, the manufacture of UHPC inevitably requires large volumes of Portland cement and ultra-low water-to-binder ratio (e.g.,

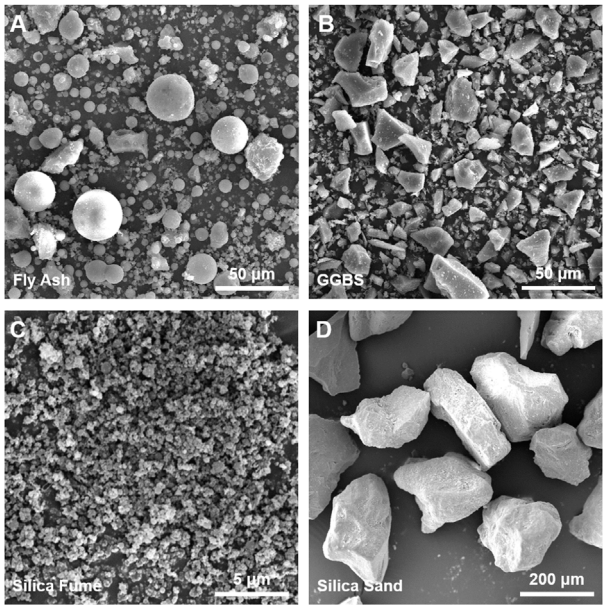

FIGURE 1
SEM images of raw materials: **(A)** Fly ash, **(B)** GGBS, **(C)** silica fume, and **(D)** silica sand.

below 0.20) (Wu et al., 2017; Yoo and Kim, 2019). Considering that Portland cement production takes up 5%–8% of the total global CO_2 emission (Scrivener and Kirkpatrick, 2008), the material sustainability of conventional UHPC is a concern, despite its excellent mechanical and durability performances. Therefore, the promotion of more sustainable binder materials for UHPC are essential.

In recent decades, geopolymer, which is known as a clinker-free low-carbon binder, has a good potential to be a sustainable replacement for Portland cement, and has gradually attracted increasing attentions of researchers (Li et al., 2019; Amran et al., 2020; Xu et al., 2021a; Peng et al., 2022; Peng et al., 2023). Since geopolymer can present a similar mechanical performance with the cement paste, it has been successfully adopted to produce different types of advanced sustainable construction materials, such as artificial geopolymer aggregates (Xu et al., 2021b; Qian et al., 2022; Qian et al., 2023), Engineered/Strain-Hardening Geopolymer Composites (EGC/SHGC) (Yoo et al., 2022b; Lao et al., 2023), and ultra-high-performance geopolymer concrete (UHPGC) (Ambily et al., 2014; Ranjbar et al., 2017; Wetzel and Middendorf, 2019; Liu et al., 2020a; Liu et al., 2020b; Lao et al., 2022). Here, it is mentioned that strain-hardening can also be achieved in UHPGC through proper matrix design and fiber utilization, and this material can be termed as strain-hardening UHPGC (SH-UHPGC) (Lao et al., 2022). The tensile strain-hardening behavior can further extend the potential of such construction materials for different application purposes (e.g., precast structure, repair, impact, and explosive resistances) (Kumar et al., 2022; Deng et al., 2023; Yin et al., 2023a; Yin et al., 2023b).

To achieve high/ultra-high compressive strength, several methods are utilized in the design and development of UHPGC. High-reactivity precursors are commonly used, and the particles of different precursors should be well-packed to form a very dense matrix. In addition, alkali activators with a proper alkalinity and silica modulus are required to provide an alkaline aqueous environment for the dissolution of precursors and the condensation of reaction products. Typical alkaline activators are sodium hydroxide (NaOH), sodium silicate (Na_2SiO_3), waterglass, or their hybridizations due to their strong alkalinity and high efficiency of activation. In this aspect, SiO_3^{2-} can participate in the formation of the reaction products by supplementing essential components for the condensation of aluminosilicate gels (Kashani et al., 2014). Also, heat curing is appreciated as it can highly promote the reaction degree of the precursors.

However, although geopolymer is considered greener than cement, the production and use of the sodium silicate (Na_2SiO_3) as alkaline activator will still contribute to comparatively high carbon emission (Habert et al., 2011), as this material is typically synthesized by dissolving silica in molten sodium carbonate at 1,400°C. Currently, the available UHPGC mixes in literature still heavily rely on silicate-based activators (Qaidi et al., 2022). Moreover, compared to normal-strength geopolymer concrete, a comparatively high precursor content is used due to the low water-to-precursor ratio, which inevitably requires a high dosage of alkalis. Therefore, it is of great significance to seek alternative greener alkaline activators for UHPGC (Alnahhal et al., 2021; Ahmad et al., 2022).

Compared to Na_2SiO_3, sodium carbonate (Na_2CO_3) can be a promising substitution with lower environmental impact, together with wide availability and chemical stability, and success has been achieved in utilizing Na_2CO_3 in the production of normal-strength geopolymer (Krivenko, 1994; Xu et al., 2008; Abdalqader et al., 2016; Akturk et al., 2019). It is noted that Na_2CO_3 is exclusively manufactured by the Solvay process, where the CO_2 in the air can even be captured and reduced (Lackner, 2002; Huijgen and Comans, 2003). However, since the reaction products in geopolymer are highly dependent on the functional group in the alkaline activator (e.g., SiO_3^{2-}, CO_3^{2-}), the characteristics of the produced Na_2CO_3-based geopolymer may differ from that of the Na_2SiO_3-based ones. For example, from the geopolymer paste study, the Na_2CO_3-based geopolymer is usually characterized by a prolonged setting time (Fernández-Jiménez and Puertas, 2001; Bernal et al., 2015; Walling et al., 2018) and extremely slow strength

TABLE 1 Mix proportions of SH-UHPGC (weight ratio).

Mix IDs	Precursors (total 1.000)			Activators			Extra water	Total water	Sand	Steel fibers
	FA	GGBS	SF	Na_2CO_3-anhydrous	Na_2SiO_3-anhydrous	Waterglass				
C100S0	0.185	0.738	0.077	0.0825	/	0.141 (Water: 0.080)	0.180	0.260	0.650	2.0 (Vol. %)
C50S50				0.0413	0.0475					
C0S100				/	0.0950					

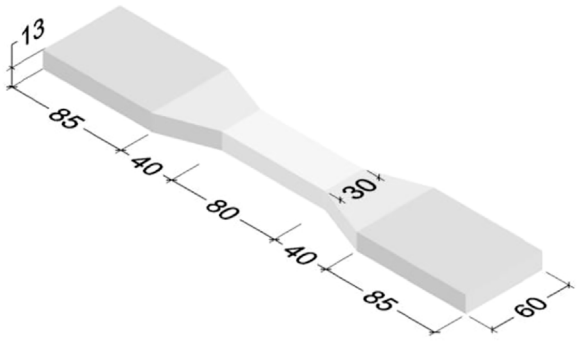

FIGURE 2
Dimensions of dumbbell specimen.

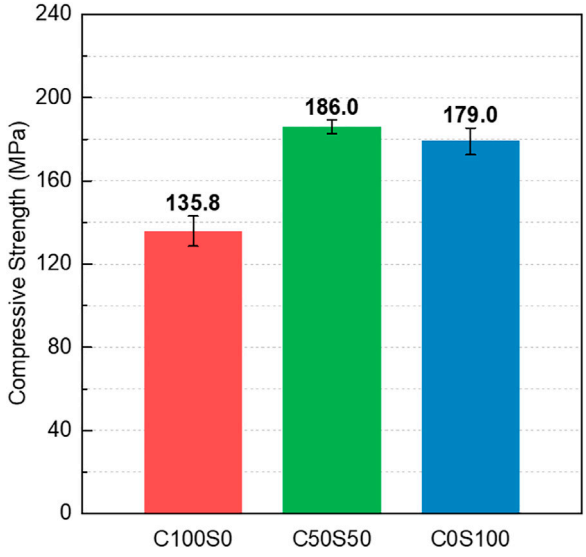

FIGURE 3
Compressive strength of SH-UHPGC with different activators.

development, as the lower alkalinity (i.e., lower PH value) and the functional group CO_3^{2-} of Na_2CO_3 will impede the formation of the hardened products (Bernal et al., 2015). In order to avoid the above drawbacks, combining Na_2CO_3 with other activators (e.g., Na_2SiO_3, $NaAlO_2$, or NaOH) (Li and Sun, 2000; Bernal et al., 2016; Ishwarya et al., 2019; Wang et al., 2021) or additives [e.g., $Ca(OH)_2$, MgO, or CaO] (Bellmann and Stark, 2009; Abdalqader et al., 2015; Wang et al., 2018) can be an effective method to reduce the setting time and even enable higher mechanical performance of geopolymers. However, up to now, almost no efforts have been tried to produce UHPGC (especially SH-UHPGC) by utilizing Na_2CO_3 as alkaline activators. To fill the knowledge gap, this study explores the feasibility of Na_2CO_3-based SH-UHPGC for the first time, and tries to understand the influence of Na_2CO_3 on the matrix characteristics, mechanical properties, and environmental impacts of SH-UHPGC.

In the following, a comprehensive investigation was performed to study the properties of SH-UHPGC with pure Na_2SiO_3, hybrid Na_2SiO_3 and Na_2CO_3, and pure Na_2CO_3 as solid alkaline activators. First, matrix characteristics including compressive strength, reaction heat, microstructures, and the chemical compositions were analyzed. Then, tensile performances and cracking behaviors of the produced SH-UHPGC were tested and compared. Finally, environmental impacts and economical potentials of the developed SH-UHPGC were performed, and the overall performance was assessed.

2 Experimental programs

2.1 Raw materials

Fly ash (FA), ground granulated blast-furnace slag (GGBS), and silica fume (SF) were used as precursors for SH-UHPGC production. The commercial fly ash and GGBS are provided by Green Island Cement Co. Ltd., Hong Kong, and silica fume is purchased from mainland China. According to X-ray fluorescence (XRF) tests, the fly ash was classified as Class F according to ASTM C618-19 (ASTM, 2019), with 52.4% SiO_2, 25.8% Al_2O_3, and 8.4% Fe_2O_3, GGBS contained 44.2% CaO, 32.1% SiO_2, and 14.1% Al_2O_3, while silica fume contained over 95% SiO_2. The three

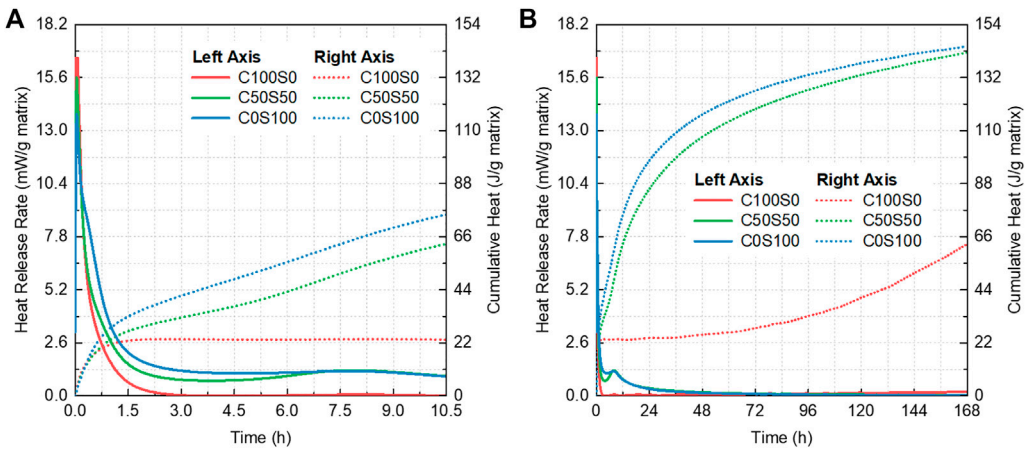

FIGURE 4
Reaction heat of SH-UHPGC pastes with different activators: **(A)** early-age reaction heat, **(B)** 7-d reaction heat.

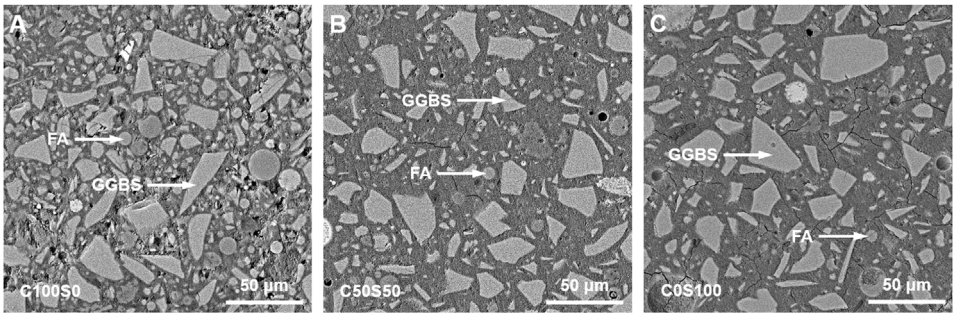

FIGURE 5
BSE images of SH-UHPGC pastes with different activators: **(A)** C100S0, **(B)** C50S50, and **(C)** C0S100.

types of precursors (i.e., FA, GGBS, and SF) have D_{50} particle sizes of 13.47 μm, 10.83 μm, and 0.56 μm, respectively. Fine silica sand was used as the aggregates in SH-UHPGC, which have an average diameter smaller than 300 μm and water absorption of 0.8%. Figure 1 presents the morphological patterns of these materials under scanning electron microscopic (SEM). Fly ash particles were mostly spherical while GGBS particles were angular, and silica fume was in a much smaller size. Two types of solid alkaline activators were adopted in this study, i.e., sodium metasilicate (Na_2SiO_3-anhydrous) and sodium carbonate (Na_2CO_3-anhydrous). Both were in analytical grade with purity over 99.5%. Besides, liquid waterglass purchased from Kowloon Sodium Silicate Factory Ltd. containing 27.7% SiO_2, 8.7% Na_2O, and 56.8% H_2O was also used as the alkaline activator in this study. Finally, straight copper-coated steel fibers with a length and diameter of 13 mm and 200 μm, respectively, were used as reinforcements to realize the tensile strain-hardening behavior of UHPGC.

2.2 Preparation of strain-hardening ultra-high-performance geopolymer concrete

The mix proportion of SH-UHPGC was adapted from the authors' previous work (Lao et al., 2022), wherein the precursor and aggregate contents were optimized by the particle packing theory to achieve the ultra-high compressive strength. With the same waterglass content, different ratios of Na_2CO_3 and Na_2SiO_3 were adopted as the variables (i.e., pure Na_2CO_3, hybrid Na_2CO_3 and Na_2SiO_3, and pure Na_2SiO_3), and the mix proportions of SH-UHPGC are summarized in Table 1. Specifically in this study, the fly ash-to-GGBS ratio was fixed at 1:4, and the water/precursor ratio was 0.26. Besides, the Na_2O/precursor ratio was fixed at 6%, and 2.0% (by volume) steel fibers were added. In the table, the Mix ID "CaSb" was used to represent the mixtures with different sodium silicate/carbonate ratios, wherein C and S represent Na_2CO_3 and Na_2SiO_3, respectively, and a and b represent their percentages. It should be noted that for C50S50 in Table 1, the mole ratio of Na_2CO_3 anhydrous and Na_2SiO_3 anhydrous was 1:1.

Before the SH-UHPGC preparation, the solid activators, waterglass, and water were mixed to form a uniform alkaline solution, which was cooled down until the room temperature was reached. For the SH-UHPGC production, precursors and sand were firstly dry-mixed for 5 min, followed by the adding of alkali solution and the continuous stirring for another 10 min. Finally, steel fibers were added and the mixture was further mixed for 5 min. After all the mixing steps were completed, the mini-slump tests were conducted to measure the flowabilities of different mixes, which were measured as 135 mm, 162 mm, and 185 mm for C100S0, C50S50, and C0S100, respectively. The flowability of SH-UHPGC decreased with higher ratio of Na_2CO_3. After that, the fresh slurry was cast into cubic and dumbbell molds, and sealed with plastic films to avoid excessive water loss. It should be noted that demolding was conducted after 7 days as the C100S0 specimens took a much longer time to set and get hardened. Then, in order to accelerate the reaction and achieve high strength, the demolded samples were sealed with plastic films and cured at 80°C in an oven for 3 days. After heat curing, the specimens were dried at room temperature (23°C) for 2 days until further tests.

2.3 Testing methods

The compressive strengths were measured by three 50 mm × 50 mm × 50 mm cubes under the loading rate of 1.0 MPa/s. The direct tensile stress-strain relationships of SH-UHPGC were tested by three dumbbell specimens (Figure 2) under a displacement-controlled rate of 0.5 mm/min (Wu et al., 2018; Wu et al., 2020). The tensile strain of the middle area (with 80 mm gauge length) was measured by two symmetrically arranged linear

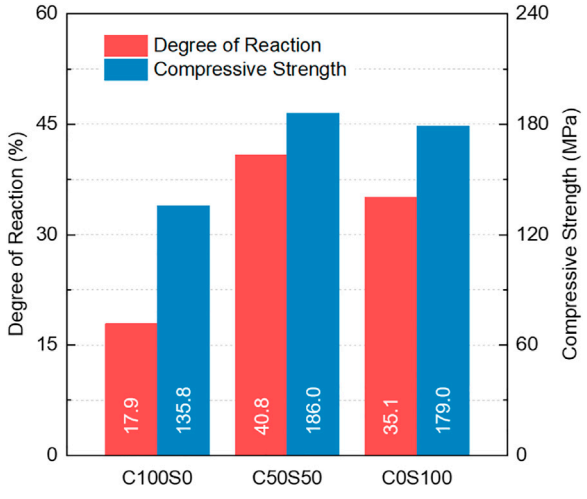

FIGURE 6
Reaction degrees of SH-UHPGC pastes with different activators.

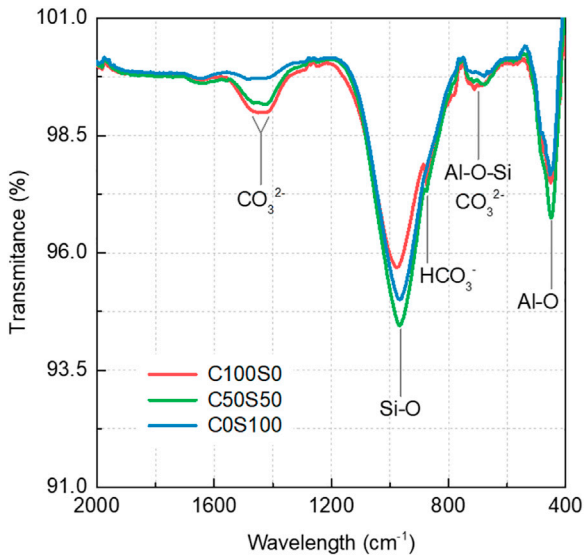

FIGURE 7
Results of FTIR analysis of SH-UHPGC pastes with different activators.

variable differential transformers (LVDTs). For digital image correlation (DIC) analysis, one side of the dumbbell specimen was sprayed with black and white spackles (Huang et al., 2017; Li et al., 2021), and this side was continuously photographed by a digital camera at an interval of 3 s during the test.

For the matrix characterization, the release of the reaction heat during the first 7 days was recorded by an isothermal calorimeter (Calmetrix I-Cal 4,000). For each mix, approximately 100 g paste sample (excluding sands and steel fibers) was stirred outside the machine for 3 min ahead of time, after which they were put in the isothermal calorimeter for 7 days for the reaction heat measurement. Then, the hardened pastes were collected and cured in the same way as described in Section 2.2, and the fragments from the inner regions were cut, fixed in epoxy, polished to obtain a smooth surface, freeze-dried at −80°C for 4 h, and coated with a gold sputter for backscattered electron (BSE) analysis (Tescan VEGA3). In the BSE test, a magnification of 1,200 times was adopted. Additionally, for Fourier-Transform Infrared Spectroscopy (FTIR) tests, fragments of the pastes were collected and pulverized into powders (smaller than 75 μm). The spectra from 400 cm^{-1} to 2000 cm^{-1} with a resolution of 4 cm^{-1} were recorded under ATR (Attenuated Total Reflection) mode.

3 Compressive strength and matrix characteristics

3.1 Compressive strength

The compressive strengths of SH-UHPGC are presented in Figure 3. All the mixes exhibited compressive strengths over 130 MPa. In the aspect of the different activators used, the compressive strength of the mix with sodium carbonate (i.e., C100S0, 135.8 MPa) was significantly lower than the mix with sodium silicate (i.e., C0S100, 179.0 MPa). Considering that the former mixture took a much longer time to set during sample preparation (up to 7 days), pure sodium carbonate showed a lower activation potential and cannot achieve rapid strength development of SH-UHPGC. Interestingly, C50S50 (186.0 MPa) with hybrid Na_2CO_3 and Na_2SiO_3 showed the highest strength among the three mixes (37.0% and 3.9% higher than those of C100S0 and C0S100, respectively). This phenomenon indicates the positive effect of combining Na_2CO_3 and Na_2SiO_3 in the alkali-activation and the mechanical performance improvement of SH-UHPGC. The mechanism of this phenomenon will be discussed in the following sections based on reaction kinetics.

3.2 Reaction heat

The 7-day reaction heat release curves of the SH-UHPGC pastes are plotted in Figure 4. Generally, the reaction heat release can be divided into five stages as proposed by Shi and Day (Shi and Day, 1995): 1) initial stage, 2) induction stage, 3) acceleration stage, 4) deceleration stage, and 5) steady-state diffusion stage. Such five-stage heat release procedure was observed in the mixture containing Na_2SiO_3 (i.e., C0S100 and C50S50), while for C100S0, the

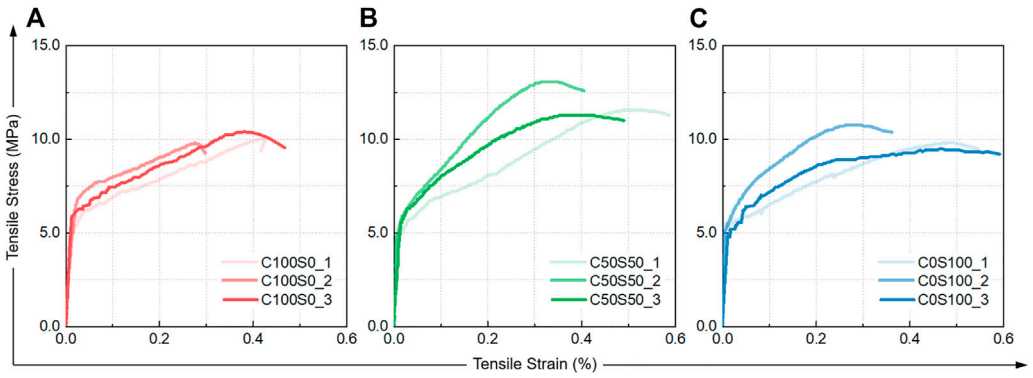

FIGURE 8
Tensile stress–strain curves of SH-UHPGC **(A)** C100S0, **(B)** C50S50, and **(C)** C0S100.

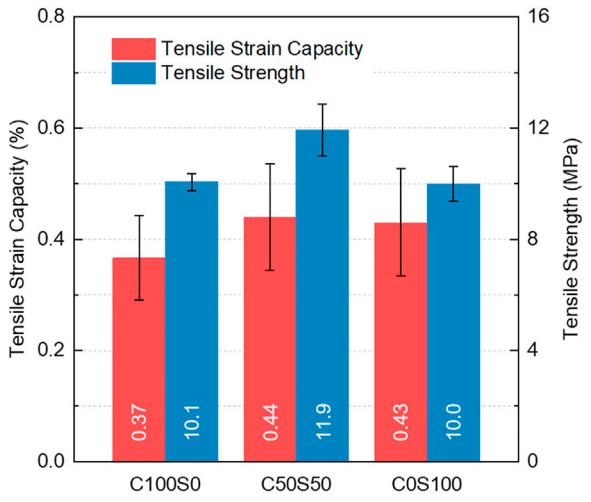

FIGURE 9
Summarized tensile performances of SH-UHPGC with different activators.

acceleration and deceleration stages were not clearly observed in the early 7 days.

To make a clearer observation, the early-age heat release procedures of different mixes in the first 10 hours are presented in Figure 4A. For the initial stage associated with the preliminary dissolution of the precursors and the initial reaction within the first hour, the heat release rate was higher as the Na_2CO_3 ratio increased. A possible reason could be that at the very early stage, the Ca^{2+} released from the precursors immediately combined with CO_3^{2-} to form $CaCO_3$ polymorphs or sodium-calcium carbonate phase (pirssonite, hydroxysodalite, and gaylussite) (Bernal et al., 2016). But for C0S100, no such phenomenon was observed due to the absence of CO_3^{2-}.

After the initial stage, C100S0 maintained an extremely slow heat release rate until the end of the test (168 h). In comparison, C50S50 showed a significant induction stage, which appeared as a concave between the initial peak and the acceleration stage in the heat release rate curve. For C0S100, however, such induction stage was less obvious, which was the major difference between C50S50 and C0S100. The induction stage corresponds to the progressive dissolution of the precursors and the initial condensation and precipitation of the reaction product. The reason may lay in the comparatively lower PH value of the hybrid activators and the fixation of Ca^{2+} ions by CO_3^{2-} in C50S50 at the early stage, which made the release of Ca^{2+} from the precursors slower, reduced its concentration in the pore solution and consequently impeded the precipitation of reaction products. However, no such phenomena occurred in C0S100 due to the absence of CO_3^{2-}.

Then, after the acceleration stage, C50S50 and C100S0 peaked almost at the same value in the heat release rate curve. After 48 h, C50S50 exhibited a higher heat release rate than that of C0S100 as the difference between their cumulative heat release curves gradually became closer. The reason for the above phenomenon is that in C50S50, the $CaCO_3$ polymorphs formed at the initial and induction stages, could act as nucleation seeds (Tan et al., 2019), promote the reaction and facilitate the formation of the reaction products. From the end of the 7-day detection, it could be forecasted that the cumulative heat release of C50S50 may exceed that of C0S100 under further curing. In comparison, the heat release rate of C100S0 showed a gradually increasing trend over time, indicating that the alkali-activation reaction would gradually take effects after the

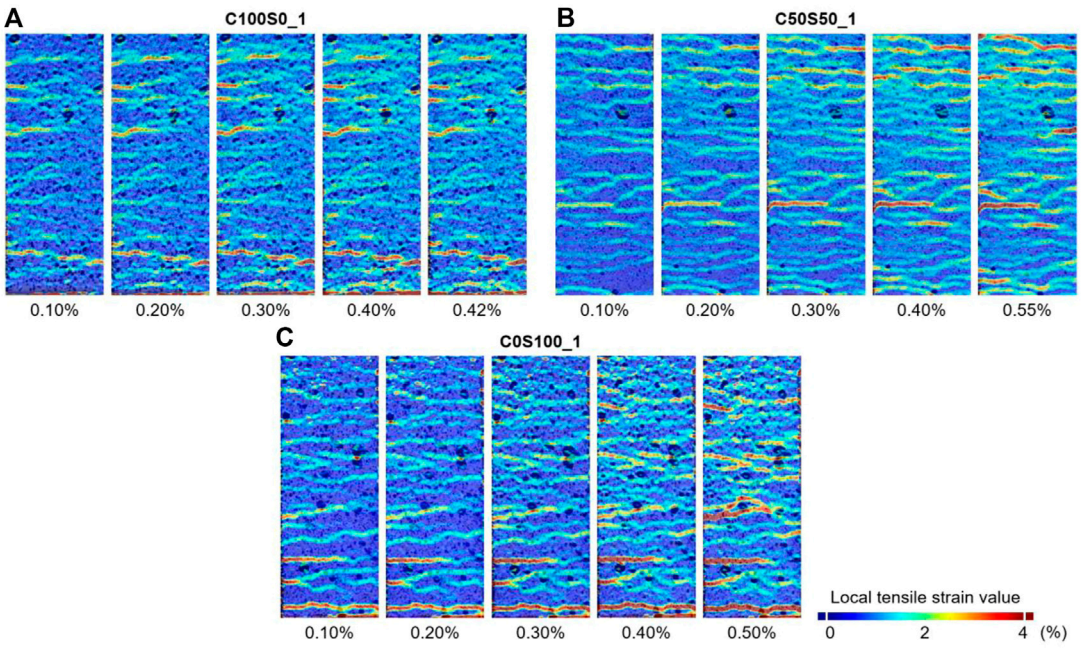

FIGURE 10
DIC strain fields of SH-UHPGC at different strain levels **(A)** C100S0, **(B)** C50S50, and **(C)** C0S100.

TABLE 2 Embodied carbon, embodied energy, and cost of raw materials.

Raw materials	Embodied carbon (metric ton eq. CO2/ metric ton)	Embodied energy (GJ/metric ton)	Cost (HKD/metric ton)
FA	0.004 Hammond and Jones (2008)	0.10 Yu et al. (2019b)	350 Xu et al. (2022b)
GGBS	0.042 Hammond and Jones (2008)	0.20 Yang et al. (2020)	500 Xu et al. (2022b)
SF	0.024 Vijayarethinam (2009)	0.10 Yu et al. (2019b)	2,100 Xu et al. (2022b)
Silica Sand	0.023 Yu et al. (2019b)	0.08 Yu et al. (2019b)	950 Xu et al. (2021c)
Na_2SiO_3	1.860 Xu et al. (2021b)	9.40 Yang et al. (2020)	860 Xu et al. (2022b)
Na_2CO_3	0.110 Yang et al. (2020)	5.80 Yang et al. (2020)	700 Yang et al. (2020)
Waterglass[a]	0.804 Xu et al. (2021b)	4.07 Yang et al. (2020)	2,266 Song et al. (2020)
Water	0.001 Yu et al. (2019b)	0.01 Yu et al. (2019b)	7 Xu et al. (2022b)
Steel Fiber	2.830 Yu et al. (2019b)	36.00 Yu et al. (2019b)	14,000 Yu et al. (2019b)

[a]Waterglass contains 56.8% H_2O in weight.

TABLE 3 Embodied carbon, embodied energy, and cost of SH-UHPGC.

Raw materials	Embodied carbon (kg CO_2/m^3)			Embodied energy (MJ/m^3)			Cost (HKD/m^3)		
	C100S0	C50S50	C0S100	C100S0	C50S50	C0S100	C100S0	C50S50	C0S100
FA	0.8	0.8	0.8	19.2	19.2	19.2	67.1	67.1	67.1
GGBS	32.2	32.2	32.2	153.2	153.2	153.2	383.1	383.1	383.1
SF	1.9	1.9	1.9	8.0	8.0	8.0	167.8	167.8	167.8
Silica Sand	15.7	15.7	15.7	54.6	54.6	54.6	640.8	640.8	640.8
Na_2SiO_3	0.0	91.6	183.2	0.0	463.0	925.9	0.0	42.4	84.7
Na_2CO_3	9.4	4.7	0.0	496.4	248.2	0.0	59.9	30.0	0.0
Waterglass	117.9	117.9	117.9	596.6	596.6	596.6	332.4	332.4	332.4
Water	0.2	0.2	0.2	1.9	1.9	1.9	1.3	1.3	1.3
Steel Fiber	441.5	441.5	441.5	5,616.0	5,616.0	5,616.0	2,184.0	2,184.0	2,184.0
Total	619.6	706.5	793.4	6,945.8	7,160.6	7,375.3	3,836.4	3,848.8	3,861.2

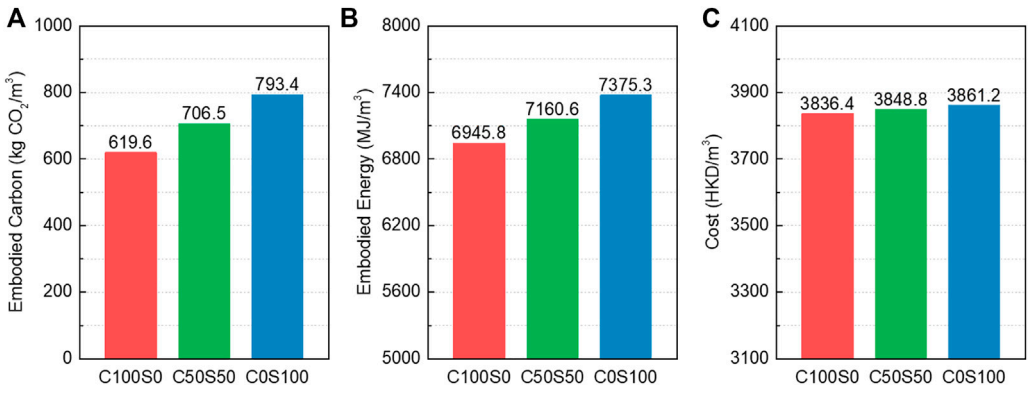

FIGURE 11
Environmental impacts and economical potentials of SH-UHPGC: **(A)** Embodied carbon, **(B)** embodied energy, and **(C)** material costs.

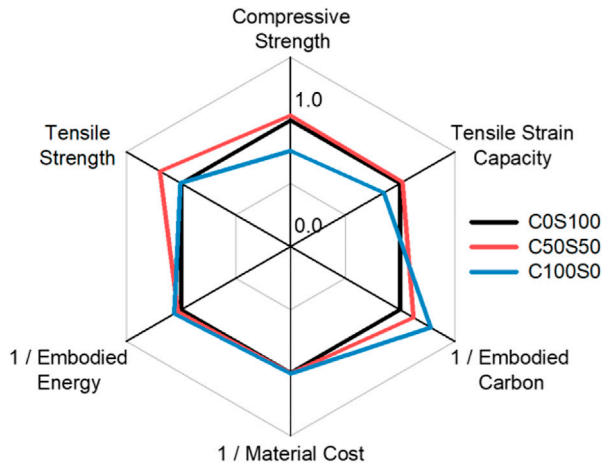

FIGURE 12
Overall assessment of SH-UHPGC considering mechanical performance, energy consumption, environmental impact, and material cost.

CO_3^{2-} was continuously consumed by the Ca^{2+} release from the precursors (Bernal et al., 2015).

3.3 Backscattered electron analysis

The microstructures of SH-UHPGC pastes with different activators observed from BSE tests are shown in Figure 5. As can be seen in all the mixes, a large number of unreacted GGBS and fly ash particles with different sizes remained in the pastes, and the dark-grey region encapsulating the unreacted particles represented the space-filling gels generated from alkali-activation. For C100S0, obviously, the number of the unreacted raw precursors seemed to be the largest, and the microstructure of the generated gels was loose and heterogeneous with some evident flaws, which is the reason for the lowest compressive strength of this mix as presented in Figure 3. In comparison, both C50S50 and C0S100 presented denser and more uniform microstructures without significant flaws and voids. Therefore, the C50S50 and C0S100 mixes with Na_2SiO_3 had a higher reaction degree than C50S50 and the reaction products both presented excellent space-filling effects as compared to C100S0.

To further illustrate the reaction conditions of SH-UHPGC pastes with different activators, the reaction degree was calculated based on the BSE images as recommended by Scrivener et al. (2016). For each mix, 15 BSE images with the dimensions of 170 μm × 230 μm were used for calculation, and the obtained results are shown in Figure 6. As observed from the figure, the reaction degrees of C50S50 and C0S100 were much higher than that of C100S0, which coincided well with the reaction heat results in Figure 4. Interestingly, a higher reaction degree was observed in C50S50 (40.8%) than that in C0S100 (35.1%). As discussed in Section 3.2, the $CaCO_3$ polymorphs, as initial products from Na_2CO_3 activation, could play as nucleation seeds and facilitate the gel formation of C50S50, which thus presents a higher degree of reaction than C0S100 under further curing. In comparison, C100S0 exhibited a reaction degree even lower than 20% (i.e., 17.9%) and was almost half that of C0S100. Therefore, such a low reaction degree of C100S0 could not provide sufficient reaction products to complete the space-filling procedure. In order to present the relationship between reaction degrees and compressive strengths of SH-UHPGC, these two indices are plotted together in Figure 6 as well. Obviously, the compressive strength showed a positive relation with the reaction degree, indicating that the adjustment of the reaction degree of the matrix is important for tailoring the compressive strengths of SH-UHPGC.

3.4 Fourier-transform infrared spectroscopy analysis

FTIR was employed to investigate the chemical composition differences of the reaction products in different mixes, and the tested results are presented in Figure 7. Baseline correction was done on all the spectra. In the figure, the intensity of the characteristic bands at around 1,421–1,470 cm^{-1} corresponds to the asymmetric stretching vibrations of ν^3 C-O bonds in CO_3^{2-}, and the intensity at around 876 cm^{-1} corresponds to the out-of-plane bending vibration of ν^2 C-O bonds in HCO_3^- (Nedeljković et al., 2018), which both tended to increase as the sodium carbonate ratio increased. Here, it is noted that the weak signals occurred in C0S100 are attributed to the unavoidable carbonation during the sample preparation. The signal of ν^4 C-O bonds in CO_3^{2-} and the bending of Al-O-Si could have overlapped at around 712 cm^{-1}. The peak centered at around 449 cm^{-1} was assigned to the bending vibrations in the Al-O octahedrons (Cao et al., 2020). The main peaks at around 970 cm^{-1} are designated to the Si-O-T (T denotes Si or Al) bonds in silicate gels, whose intensity was highest in C50S50, followed by C0S100 and C100S0 in sequence. This result is in accordance with the findings in reaction heat and BSE observations, which may further validate the enhanced alkali-activation reaction degree in SH-UHPGC with hybrid Na_2CO_3 and Na_2SiO_3 activators.

4 Tensile performance and cracking behavior

4.1 Tensile performance

The tensile stress–strain curves of SH-UHPGC with different matrices are presented in Figure 8. Obviously, strain-hardening behaviors were observed in all the mixes (i.e., tensile strength could further increase after the first cracking strength, together with the increase of tensile strain). Unlike ECC materials showing multiple stress drops in tensile responses (Yu et al., 2020; Xu et al., 2022a; Li et al., 2023; Xu et al., 2023), the tensile stress-strain curves of SH-UHPGC were very smooth, indicating the excellent crack width control ability of steel fibers (Lao et al., 2022). To further analyze the tensile performances of SH-UHPGC, their tensile strengths and strain capacities are summarized in Figure 9. From the figure, the highest tensile strain capacity (0.44%) and tensile strength (11.9 MPa) were achieved in C50S50, indicating the excellent tensile performance of the mix using hybrid Na_2SiO_3 and Na_2CO_3 activators. Considering that the tensile strength of strain-hardening cementitious (geopolymer) composites is highly dependent on the fiber/matrix bond (Lao et al., 2023), the highest tensile strength of C50S50 can be attributed to the highest reaction degree of the matrix (as presented in Figure 6). In

comparison, the other two mixes showed similar tensile strengths, and C100S0 presented the lowest tensile strain capacity (0.37%), indicating that Na_2SiO_3 showed better activation effect than Na_2CO_3 in producing SH-UHPGC.

4.2 Digital image correlation strain fields

The DIC analysis was performed on a subset radius and subset spacing of 30 pixels and 3 pixels, respectively. The local strain value was calculated based on a strain radius of 3 pixels. Figure 10 presents the DIC strain fields of SH-UHPGC at different strain levels under direct tension. Here, four constant strain levels (i.e., 0.10%, 0.20%, 0.30%, and 0.40%) and the ultimate strain were adopted for analysis. From the figure, for all the SH-UHPGC mixes, multiple cracks were observed at all the presented strain levels, and the cracking became more saturated as the strain level increased. It should be highlighted that very significant multiple cracking can be observed for all the developed SH-UHPGC even at a very low tensile strain level (e.g., 0.1% or 0.2%). This phenomenon is quite different from those of cement-based strain-hardening UHPC and high/ultra-high-strength ECC, which only showed few cracks with the tensile strain lower than 0.2% (Huang et al., 2021b; Huang et al., 2021c; Huang et al., 2022b; Zhu et al., 2022). For the developed SH-UHPGC, the steel fibers used can effectively narrow the crack widths (i.e., below 30 μm). However, the tensile crack width of ECC/SHCC is commonly 60–150 μm (Ding et al., 2018; Yu et al., 2019a; Huang et al., 2019). Thus, at the same tensile strain level, the crack number of SH-UHPGC would be much larger than that of ECC/SHCC, leading to the pronounced multiple-cracking behavior of SH-UHPGC.

Due to the limitation of the digital camera used, the maximum resolution of the captured photographs was not enough for the analysis of crack width, and thus no visible cracks could be found in the photographs at different strain levels. It indicated that the crack widths of the developed SH-UHPGC should be smaller than 30 μm, as 1 pixel = 30 μm in the captured photographs. The actual value of the crack width of SH-UHPGC in this study remains unknown, and it should be further investigated in the following work.

5 Environmental impacts and economical potentials

5.1 Embodied carbon, embodied energy, and material costs

Although geopolymer is generally regarded as a green material owing to its clinker-free feature, the use of conventionally adopted alkaline activator (e.g., Na_2SiO_3) still shows a heavy impact on the environment from life-cycle assessments (Habert et al., 2011). Therefore, it is of great significance to evaluate the environmental impact and economical potential of replacing Na_2SiO_3 with Na_2CO_3 in the production of SH-UHPGC.

The embodied carbon, embodied energy, and costs of raw materials and the produced SH-UHPGC are summarized in Table 2 and Table 3, respectively. In addition, the results of SH-UHPGC with different matrices are presented in Figure 11 for a more distinctive comparison. It can be found in Table 2 that Na_2SiO_3 shows higher embodied carbon, embodied energy, and material cost than Na_2CO_3. In consequence, when the replacement ratio of Na_2SiO_3 by Na_2CO_3 increased from 0% to 100% to produce SH-UHPGC, the embodied carbon decreased from 793.4 kg CO_2/m^3 to 619.6 kg CO_2/m^3 and the embodied energy decreased from 7,375.3 MJ/m^3 to 6,945.8 MJ/m^3, while the material cost changed very little. Therefore, the Na_2CO_3-based SH-UHPGC shows better sustainability and is more eco-friendly than the Na_2SiO_3-based one. Also, among all the raw materials of SH-UHPGC, it is mentioned that the use of steel fibers made heavy contributions to the three indices (i.e., 55.6%–71.3% of the total embodied carbon, 76.1%–80.9% of the total embodied energy, and 56.6%–56.9% of the total material cost). In this aspect, it is meaningful to seek for alternative fibers to realize tensile strain-hardening behavior of greener and cheaper UHPGC in the future.

5.2 Overall assessment

Based on the results in the above sections, an overall assessment was conducted considering mechanical performances, environmental impacts, and material costs. A radar graph was used to present the results (i.e., Figure 12). Here, because lower embodied carbon, embodied energy, and material cost are desirable for the practical applications of UHPGC, their reciprocals were used in the six-dimensional presentation. For easy comparison, all values are normalized by the corresponding value of C0S100. Among the three mixes, C100S0 was the most environmentally friendly, but presented the poorest mechanical performances. In comparison, C50S50 showed the most distinguished tensile strain capacity, tensile strength, and compressive strength, and a moderate environmental impact, demonstrating the superiority of this mix. For C0S100, although its mechanical performance is also excellent, this mix showed the highest embodied carbon, as well as comparatively high embodied energy and material cost. Therefore, the use of hybrid Na_2SiO_3 and Na_2CO_3 is a promising method to achieve the best overall performance of the developed SH-UHPGC.

6 Conclusion

In this study, Na_2CO_3 was used to replace the Na_2SiO_3 partially or fully in strain-hardening ultra-high performance geopolymer concrete (SH-UHPGC) production. A comprehensive investigation was conducted to study the mechanical performances and reaction mechanisms, and an environmental and cost analysis was also conducted. From the obtained results, main conclusions can be drawn as follows.

- Among the three mixes, SH-UHPGC with hybrid activators showed the highest compressive strength (186.0 MPa), while that activated by Na_2CO_3 presented the lowest strength. From the reaction heat results, SH-UHPGC with hybrid activators presented the highest heat release rate at the later stage, while that of SH-UHPGC with pure Na_2CO_3 was very slow, although it showed a gradually increasing trend over time. In the aspect of

BSE observations, SH-UHPGC with pure Na_2CO_3 showed a loose and heterogeneous microstructure and the lowest reaction degree, and the highest reaction degree was found in SH-UHPGC with hybrid activators. FTIR results further demonstrated the high reaction efficiency of SH-UHPGC with hybrid activators.

- Strain-hardening and multiple cracking were achieved in all the SH-UHPGC mixes. The highest tensile strain capacity (0.44%) and tensile strength (11.9 MPa) were achieved in SH-UHPGC with hybrid activators, which is accordance with the findings in reaction procedure and product analysis. In comparison, the other two mixes showed similar tensile strengths. It should be highlighted that very significant multiple cracking can be observed for all the SH-UHPGC even at a very low tensile strain level (e.g., 0.1%).
- SH-UHPGC with pure Na_2CO_3 showed the lowest embodied carbon, embodied energy, and material costs, indicating an excellent potential of using Na_2CO_3 as activator in SH-UHPGC production. In addition, SH-UHPGC with hybrid Na_2SiO_3 and Na_2CO_3 presented the best overall performance, considering the mechanical properties, energy consumption, environmental impact, and economical potential.

Na_2CO_3 has been successfully used in producing green SH-UHPGC. However, several limitations still exist in the Na_2CO_3-based SH-UHPGC. At the current stage, SH-UHPGC still need heat curing for achieving a high early strength, which hinders the application in practical constructions. Furthermore, Na_2SiO_3 cannot be fully replaced by Na_2CO_3 considering the unacceptable setting time and compromised performance. Finally, steel fibers used in SH-UHPGC inevitably brought the largest proportion of material cost, carbon emission, and energy consumption. In the following studies, additional efforts are needed to further optimize this material.

It is worth mentioning that in the previous work, the authors have successfully designed and developed steel-fiber-reinforced SH-UHPGC with an ultra-high compressive strength up to 220 MPa and PE-fiber-reinforced SH-UHPGC [or Ultra-High-Strength Engineered Geopolymer Composites, (UHS-EGC)] with compressive strength over 180 MPa and tensile strain capacity over 9%. Detailed information can be found in Lao et al. (2022), Lao et al. (2023).

Data availability statement

The raw data supporting the conclusion of this article will be made available by the authors, without undue reservation.

Author contributions

J-CL: Conceptualization, Investigation, Validation, Writing—Original Draft. L-YX: Investigation, Formal analysis, Writing—Original Draft. B-TH: Conceptualization, Methodology, Formal analysis, Visualization, Writing—Review and Editing. J-XZ: Validation, Formal analysis—Review and Editing. MK: Visualization, Writing—Review and Editing. J-GD: Funding Acquisition, Project administration, Supervision, Writing—Review and Editing.

Acknowledgments

The authors would like to acknowledge the financial support received from the Chinese Guangdong Province R&D Plan for Key Areas (No. 2019B111107002), the Hong Kong Research Grants Council (No. T22-502/18-R), and The Hong Kong Polytechnic University through the Research Institute for Land and Space (No. CD7D).

Conflict of interest

The authors declare that the research was conducted in the absence of any commercial or financial relationships that could be construed as a potential conflict of interest.

Publisher's note

References

Abdalqader, A. F., Jin, F., and Al-Tabbaa, A. (2015). Characterisation of reactive magnesia and sodium carbonate-activated fly ash/slag paste blends. *Constr. Build. Mater.* 93, 506–513. doi:10.1016/j.conbuildmat.2015.06.015

Abdalqader, A. F., Jin, F., and Al-Tabbaa, A. (2016). Development of greener alkali-activated cement: Utilisation of sodium carbonate for activating slag and fly ash mixtures. *J. Clean. Prod.* 113, 66–75. doi:10.1016/j.jclepro.2015.12.010

Ahmad, M. R., Lao, J., Dai, J. G., Xuan, D., and Poon, C. S. (2022). Upcycling of air pollution control residue waste into cementitious product through geopolymerization technology. *Resour. Conservation Recycl.* 181, 106231. doi:10.1016/j.resconrec.2022.106231

Akturk, B., Nayak, S., Das, S., and Kizilkanat, A. B. (2019). Microstructure and strength development of sodium carbonate–activated blast furnace slags. *J. Mater. Civ. Eng.* 31 (11), 04019283. doi:10.1061/(asce)mt.1943-5533.0002944

Alnahhal, M. F., Kim, T., and Hajimohammadi, A. (2021). Waste-derived activators for alkali-activated materials: A review. *Cem. Concr. Compos.* 118, 103980. doi:10.1016/j.cemconcomp.2021.103980

Ambily, P. S., Ravisankar, K., Umarani, C., Dattatreya, J. K., and Iyer, N. R. (2014). Development of ultra-high-performance geopolymer concrete. *Mag. Concr. Res.* 66 (2), 82–89. doi:10.1680/macr.13.00057

Amran, Y. M., Alyousef, R., Alabduljabbar, H., and El-Zeadani, M. (2020). Clean production and properties of geopolymer concrete; A review. *J. Clean. Prod.* 251, 119679. doi:10.1016/j.jclepro.2019.119679

ASTM (2019). *Standard specification for coal fly ash and raw or calcined natural pozzolan for use in concrete*. West Conshohocken, PA: ASTM International.

Bellmann, F., and Stark, J. (2009). Activation of blast furnace slag by a new method. *Cem. Concr. Res.* 39 (8), 644–650. doi:10.1016/j.cemconres.2009.05.012

Bernal, S. A., Nicolas, R. S., van Deventer, J. S., and Provis, J. L. (2016). Alkali-activated slag cements produced with a blended sodium carbonate/sodium silicate activator. *Adv. Cem. Res.* 28 (4), 262–273. doi:10.1680/jadcr.15.00013

Bernal, S. A., Provis, J. L., Myers, R. J., San Nicolas, R., and van Deventer, J. S. (2015). Role of carbonates in the chemical evolution of sodium carbonate-activated slag binders. *Mater. Struct.* 48 (3), 517–529. doi:10.1617/s11527-014-0412-6

Cao, R., Zhang, S., Banthia, N., Zhang, Y., and Zhang, Z. (2020). Interpreting the early-age reaction process of alkali-activated slag by using combined embedded ultrasonic measurement, thermal analysis, XRD, FTIR and SEM. *Compos. Part B Eng.* 186, 107840. doi:10.1016/j.compositesb.2020.107840

Deng, B. Y., Li, L. Z., Tan, D., Uddin, M. N., Cai, Z. W., Yu, K. Q., et al. (2023). Sustainable and cost-effective ultra-lightweight engineered cementitious composite: Design and material characterization. *Cement and Concrete Composites* 136, 104895

Deng, B. Y., Tan, D., Li, L. Z., Zhang, Z., Cai, Z. W., Yu, K. Q., et al. (2023). Flexural behavior of precast ultra-lightweight ECC-concrete composite slab with lattice girders. *Engineering Structures* 279, 115553

Ding, Y., Yu, K. Q., Yu, J. T., and Xu, S. L. (2018). Structural behaviors of ultra-high performance engineered cementitious composites (UHP-ECC) beams subjected to bending-experimental study. *Constr. Build. Mater.* 177, 102–115. doi:10.1016/j.conbuildmat.2018.05.122

Fernández-Jiménez, A., and Puertas, F. (2001). Setting of alkali-activated slag cement. Influence of activator nature. *Adv. Cem. Res.* 13 (3), 115–121. doi:10.1680/adcr.2001.13.3.115

Habert, G., De Lacaillerie, J. D. E., and Roussel, N. (2011). An environmental evaluation of geopolymer based concrete production: Reviewing current research trends. *J. Clean. Prod.* 19 (11), 1229–1238. doi:10.1016/j.jclepro.2011.03.012

Hammond, G. P., and Jones, C. I. (2008). Embodied energy and carbon in construction materials. *Proc. Institution Civ. Engineers-Energy* 161 (2), 87–98. doi:10.1680/ener.2008.161.2.87

Huang, B. T., Dai, J. G., Weng, K. F., Zhu, J. X., and Shah, S. P. (2021a). Flexural performance of UHPC–concrete–ECC composite member reinforced with perforated steel plates. *J. Struct. Eng.* 147 (6), 04021065. doi:10.1061/(asce)st.1943-541x.0003034

Huang, B. T., Li, Q. H., Xu, S. L., and Li, C. F. (2017). Development of reinforced ultra-high toughness cementitious composite permanent formwork: Experimental study and digital image correlation analysis. *Compos. Struct.* 180, 892–903. doi:10.1016/j.compstruct.2017.08.016

Huang, B. T., Li, Q. H., Xu, S. L., and Zhang, L. (2019). Static and fatigue performance of reinforced concrete beam strengthened with strain-hardening fiber-reinforced cementitious composite. *Eng. Struct.* 199, 109576. doi:10.1016/j.engstruct.2019.109576

Huang, B. T., Wang, Y. T., Wu, J. Q., Yu, J., Dai, J. G., and Leung, C. K. (2021c). Effect of fiber content on mechanical performance and cracking characteristics of ultra-high-performance seawater sea-sand concrete (UHP-SSC). *Adv. Struct. Eng.* 24 (6), 1182–1195. doi:10.1177/1369433220972452

Huang, B. T., Wu, J. Q., Yu, J., Dai, J. G., Leung, C. K., and Li, V. C. (2021b). Seawater sea-sand engineered/strain-hardening cementitious composites (ECC/SHCC): Assessment and modeling of crack characteristics. *Cem. Concr. Res.* 140, 106292. doi:10.1016/j.cemconres.2020.106292

Huang, B. T., Zhu, J. X., Weng, K. F., Huang, J. Q., and Dai, J. G. (2022a). Prefabricated UHPC-concrete-ECC underground utility tunnel reinforced by perforated steel plate: Experimental and numerical investigations. *Case Stud. Constr. Mater.* 16, e00856. doi:10.1016/j.cscm.2021.e00856

Huang, B. T., Zhu, J. X., Weng, K. F., Li, V. C., and Dai, J. G. (2022b). Ultra-high-strength engineered/strain-hardening cementitious composites (ECC/SHCC): Material design and effect of fiber hybridization. *Cem. Concr. Compos.* 129, 104464. doi:10.1016/j.cemconcomp.2022.104464

Huijgen, W. J. J., and Comans, R. N. J. (2003). *Carbon dioxide sequestration by mineral carbonation*. Berlin, Germany: Springer.

Ishwarya, G. A., Singh, B., Deshwal, S., and Bhattacharyya, S. K. (2019). Effect of sodium carbonate/sodium silicate activator on the rheology, geopolymerization and strength of fly ash/slag geopolymer pastes. *Cem. Concr. Compos.* 97, 226–238. doi:10.1016/j.cemconcomp.2018.12.007

Jang, Y. S., Oh, T., Banthia, N., and Yoo, D. Y. (2022). Effects of nano-SiO2 coating and induced corrosion of steel fiber on the interfacial bond and tensile properties of ultra-high-performance concrete (UHPC). *J. Build. Eng.* 54, 104637. doi:10.1016/j.jobe.2022.104637

Kashani, A., Provis, J. L., Qiao, G. G., and van Deventer, J. S. (2014). The interrelationship between surface chemistry and rheology in alkali activated slag paste. *Constr. Build. Mater.* 65, 583–591. doi:10.1016/j.conbuildmat.2014.04.127

Khan, M., Lao, J., and Dai, J. G. (2022). Comparative study of advanced computational techniques for estimating the compressive strength of UHPC. *J. Asian Concr. Fed.* 8 (1), 51–68. doi:10.18702/acf.2022.6.8.1.51

Krivenko, P. V. (1994). "Alkaline cements," in Proceedings of the 1st International Conference on Alkaline Cements and Concretes, Kiev, Ukraine, 11 June 1994. (Kiev, Ukraine: VIPOL Stock Company), 11–129.

Kumar, S., Das, C. S., Lao, J., Alrefaei, Y., and Dai, J. G. (2022). Effect of sand content on bond performance of engineered geopolymer composites (EGC) repair material. *Constr. Build. Mater.* 328, 127080. doi:10.1016/j.conbuildmat.2022.127080

Lackner, K. S. (2002). Carbonate chemistry for sequestering fossil carbon. *Annu. Rev. energy Environ.* 27 (1), 193–232. doi:10.1146/annurev.energy.27.122001.083433

Lao, J. C., Huang, B. T., Fang, Y., Xu, L. Y., Dai, J. G., and Shah, S. P. (2023). Strain-hardening alkali-activated fly ash/slag composites with ultra-high compressive strength and ultra-high tensile ductility. *Cem. Concr. Res.* 165, 107075. doi:10.1016/j.cemconres.2022.107075

Lao, J. C., Xu, L. Y., Huang, B. T., Dai, J. G., and Shah, S. P. (2022). Strain-hardening ultra-high-performance geopolymer concrete (UHPGC): Matrix design and effect of steel fibers. *Compos. Commun.* 30, 101081. doi:10.1016/j.coco.2022.101081

Li, N., Shi, C., Zhang, Z., Wang, H., and Liu, Y. (2019). A review on mixture design methods for geopolymer concrete. *Compos. Part B Eng.* 178, 107490. doi:10.1016/j.compositesb.2019.107490

Li, Q. H., Yin, X., Huang, B. T., Luo, A. M., Lyu, Y., Sun, C. J., et al. (2021). Shear interfacial fracture of strain-hardening fiber-reinforced cementitious composites and concrete: A novel approach. *Eng. Fract. Mech.* 253, 107849. doi:10.1016/j.engfracmech.2021.107849

Li, S., Chan, T. M., and Young, B. (2023). Experimental investigation on axial compressive behavior of novel FRP-ECC-HSC composite short column. *Compos. Struct.* 303, 116285. doi:10.1016/j.compstruct.2022.116285

Li, V. C. (2019). *Engineered cementitious composites (ECC)* - bendable Concrete for Sustainable and resilient infrastructure. Berlin, Heidelberg: Springer.

Li, Y., and Sun, Y. (2000). Preliminary study on combined-alkali–slag paste materials. *Cem. Concr. Res.* 30 (6), 963–966. doi:10.1016/s0008-8846(00)00269-6

Liu, Y., Shi, C., Zhang, Z., Li, N., and Shi, D. (2020). Mechanical and fracture properties of ultra-high performance geopolymer concrete: Effects of steel fiber and silica fume. *Cem. Concr. Compos.* 112, 103665. doi:10.1016/j.cemconcomp.2020.103665

Liu, Y., Zhang, Z., Shi, C., Zhu, D., Li, N., and Deng, Y. (2020). Development of ultra-high performance geopolymer concrete (UHPGC): Influence of steel fiber on mechanical properties. *Cem. Concr. Compos.* 112, 103670. doi:10.1016/j.cemconcomp.2020.103670

Nedeljković, M., Zuo, Y., Arbi, K., and Ye, G. (2018). Carbonation resistance of alkali-activated slag under natural and accelerated conditions. *J. Sustain. Metallurgy* 4 (1), 33–49. doi:10.1007/s40831-018-0166-4

Peng, K. D., Huang, B. T., Xu, L. Y., Hu, R. L., and Dai, J. G. (2022). Flexural strengthening of reinforced concrete beams using geopolymer-bonded small-diameter CFRP bars. *Eng. Struct.* 256, 113992. doi:10.1016/j.engstruct.2022.113992

Peng, K. D., Huang, J. Q., Huang, B. T., Xu, L. Y., and Dai, J. G. (2023). Shear strengthening of reinforced concrete beams using geopolymer-bonded small-diameter FRP bars. *Compos. Struct.* 305, 116513. doi:10.1016/j.compstruct.2022.116513

Qaidi, S. M., Atrushi, D. S., Mohammed, A. S., Ahmed, H. U., Faraj, R. H., Emad, W., et al. (2022). Ultra-high-performance geopolymer concrete: A review. *Constr. Build. Mater.* 346, 128495. doi:10.1016/j.conbuildmat.2022.128495

Qian, L. P., Huang, B. T., Xu, L. Y., and Dai, J. G. (2023). Concrete made with high-strength artificial geopolymer aggregates: Mechanical properties and failure mechanisms. *Constr. Build. Mater.* 367, 130318. doi:10.1016/j.conbuildmat.2023.130318

Qian, L. P., Xu, L. Y., Huang, B. T., and Dai, J. G. (2022). Pelletization and properties of artificial lightweight geopolymer aggregates (GPA): One-part vs. two-part geopolymer techniques. *J. Clean. Prod.* 374, 133933. doi:10.1016/j.jclepro.2022.133933

Ranjbar, N., Mehrali, M., Maheri, M. R., and Mehrali, M. (2017). Hot-pressed geopolymer. *Cem. Concr. Res.* 100, 14–22. doi:10.1016/j.cemconres.2017.05.010

Scrivener, K. L., and Kirkpatrick, R. J. (2008). Innovation in use and research on cementitious material. *Cem. Concr. Res.* 38 (2), 128–136. doi:10.1016/j.cemconres.2007.09.025

Scrivener K., Snellings R., and Lothenbach B. (Editors) (2016). *A practical guide to microstructural analysis of cementitious materials* (Boca Raton, FL, USA: CRC Press).

Shi, C., and Day, R. L. (1995). A calorimetric study of early hydration of alkali-slag cements. *Cem. Concr. Res.* 25 (6), 1333–1346. doi:10.1016/0008-8846(95)00126-w

Song, Y., Li, Z., Zhang, J., Tang, Y., Ge, Y., and Cui, X. (2020). A low-cost biomimetic heterostructured multilayer membrane with geopolymer microparticles for broad-spectrum water purification. *ACS Appl. Mater. Interfaces* 12 (10), 12133–12142. doi:10.1021/acsami.0c00440

Tan, H., Deng, X., He, X., Zhang, J., Zhang, X., Su, Y., et al. (2019). Compressive strength and hydration process of wet-grinded granulated blast-furnace slag activated by sodium sulfate and sodium carbonate. *Cem. Concr. Compos.* 97, 387–398. doi:10.1016/j.cemconcomp.2019.01.012

Vijayarethinam, N. (2009). Silica fume applications. *World Cem.* 40, 97–100.

Walling, S. A., Bernal, S. A., Gardner, L. J., Kinoshita, H., and Provis, J. L. (2018). Blast furnace slag-Mg (OH) 2 cements activated by sodium carbonate. *RSC Adv.* 8 (41), 23101–23118. doi:10.1039/c8ra03717e

Wang, J., Lyu, X., Wang, L., Cao, X., Liu, Q., and Zang, H. (2018). Influence of the combination of calcium oxide and sodium carbonate on the hydration reactivity of alkali-activated slag binders. *J. Clean. Prod.* 171, 622–629. doi:10.1016/j.jclepro.2017.10.077

Wang, Y. S., Alrefaei, Y., and Dai, J. G. (2021). Roles of hybrid activators in improving the early-age properties of one-part geopolymer pastes. *Constr. Build. Mater.* 306, 124880. doi:10.1016/j.conbuildmat.2021.124880

Wetzel, A., and Middendorf, B. (2019). Influence of silica fume on properties of fresh and hardened ultra-high performance concrete based on alkali-activated slag. *Cem. Concr. Compos.* 100, 53–59. doi:10.1016/j.cemconcomp.2019.03.023

Wu, H. L., Du, Y. J., Yu, J., Yang, Y. L., and Li, V. C. (2020). Hydraulic conductivity and self-healing performance of engineered cementitious composites exposed to acid mine drainage. *Sci. Total Environ.* 716, 137095. doi:10.1016/j.scitotenv.2020.137095

Wu, H. L., Zhang, D., Ellis, B. R., and Li, V. C. (2018). Development of reactive MgO-based Engineered Cementitious Composite (ECC) through accelerated carbonation curing. *Constr. Build. Mater.* 191, 23–31. doi:10.1016/j.conbuildmat.2018.09.196

Wu, H., Yu, J., Du, Y., and Li, V. C. (2021b). Mechanical performance of MgO-doped engineered cementitious composites (ECC). *Cem. Concr. Compos.* 115, 103857. doi:10.1016/j.cemconcomp.2020.103857

Wu, H., Zhang, D., Ellis, B. R., and Li, V. C. (2021a). Mechanical behavior of carbonated MgO-based Engineered Cementitious Composite (ECC) after high temperatures exposure. *Cem. Concr. Compos.* 124, 104255. doi:10.1016/j.cemconcomp.2021.104255

Wu, Z., Shi, C., He, W., and Wang, D. (2017). Static and dynamic compressive properties of ultra-high performance concrete (UHPC) with hybrid steel fiber reinforcements. *Cem. Concr. Compos.* 79, 148–157. doi:10.1016/j.cemconcomp.2017.02.010

Xiang, Y., Fang, Z., Wang, C., Zhang, Y., and Fang, Y. (2017). Experimental investigations on impact behavior of CFRP cables under pretension. *J. Compos. Constr.* 21 (2), 04016087. doi:10.1061/(asce)cc.1943-5614.0000745

Xu, H., Provis, J. L., van Deventer, J. S., and Krivenko, P. V. (2008). Characterization of aged slag concretes. *ACI Mater. J.* 105 (2), 131.

Xu, L. Y., Alrefaei, Y., Wang, Y. S., and Dai, J. G. (2021a). Recent advances in molecular dynamics simulation of the NASH geopolymer system: Modeling, structural analysis, and dynamics. *Constr. Build. Mater.* 276, 122196. doi:10.1016/j.conbuildmat.2020.122196

Xu, L. Y., Huang, B. T., and Dai, J. G. (2021c). Development of engineered cementitious composites (ECC) using artificial fine aggregates. *Constr. Build. Mater.* 305, 124742. doi:10.1016/j.conbuildmat.2021.124742

Xu, L. Y., Huang, B. T., Lan-Ping, Q., and Dai, J. G. (2022b). Enhancing long-term tensile performance of Engineered Cementitious Composites (ECC) using sustainable artificial geopolymer aggregates. *Cem. Concr. Compos.* 133, 104676. doi:10.1016/j.cemconcomp.2022.104676

Xu, L. Y., Huang, B. T., Lao, J. C., and Dai, J. G. (2022a). Tailoring strain-hardening behavior of high-strength Engineered Cementitious Composites (ECC) using hybrid silica sand and artificial geopolymer aggregates. *Mater. Des.* 220, 110876. doi:10.1016/j.matdes.2022.110876

Xu, L. Y., Huang, B. T., Lao, J. C., Yao, J., Li, V. C., and Dai, J. G. (2023). Tensile oversaturated cracking of ultra-high-strength engineered cementitious composites (UHS-ECC) with artificial geopolymer aggregates. *Cem. Concr. Compos.* 136, 104896. doi:10.1016/j.cemconcomp.2022.104896

Xu, L. Y., Qian, L. P., Huang, B. T., and Dai, J. G. (2021b). Development of artificial one-part geopolymer lightweight aggregates by crushing technique. *J. Clean. Prod.* 315, 128200. doi:10.1016/j.jclepro.2021.128200

Yang, T., Zhang, Z., Zhang, F., Gao, Y., and Wu, Q. (2020). Chloride and heavy metal binding capacities of hydrotalcite-like phases formed in greener one-part sodium carbonate-activated slag cements. *J. Clean. Prod.* 253, 120047. doi:10.1016/j.jclepro.2020.120047

Yin, X., Li, Q., Chen, B., and Xu, S. (2023b). An improved calibration of Karagozian and Case concrete/cementitious model for strain-hardening fibre-reinforced cementitious composites under explosion and penetration loadings. *Cem. Concr. Compos.* 137, 104911. doi:10.1016/j.cemconcomp.2022.104911

Yin, X., Li, Q., Xu, X., Chen, B., Guo, K., and Xu, S. (2023a). Investigation of continuous surface cap model (CSCM) for numerical simulation of strain-hardening fibre-reinforced cementitious composites against low-velocity impacts. *Compos. Struct.* 304, 116424. doi:10.1016/j.compstruct.2022.116424

Yoo, D. Y., Banthia, N., Kang, S. T., and Yoon, Y. S. (2016). Size effect in ultra-high-performance concrete beams. *Eng. Fract. Mech.* 157, 86–106. doi:10.1016/j.engfracmech.2016.02.009

Yoo, D. Y., and Kim, S. (2019). Comparative pullout behavior of half-hooked and commercial steel fibers embedded in UHPC under static and impact loads. *Cem. Concr. Compos.* 97, 89–106. doi:10.1016/j.cemconcomp.2018.12.023

Yoo, D. Y., Lee, S. K., You, I., Oh, T., Lee, Y., and Zi, G. (2022b). Development of strain-hardening geopolymer mortar based on liquid-crystal display (LCD) glass and blast furnace slag. *Constr. Build. Mater.* 331, 127334. doi:10.1016/j.conbuildmat.2022.127334

Yoo, D. Y., Oh, T., and Banthia, N. (2022a). Nanomaterials in ultra-high-performance concrete (UHPC)–A review. *Cem. Concr. Compos.* 134, 104730. doi:10.1016/j.cemconcomp.2022.104730

Yu, J., Chen, Y., and Leung, C. K. (2019b). Mechanical performance of Strain-Hardening Cementitious Composites (SHCC) with hybrid polyvinyl alcohol and steel fibers. *Compos. Struct.* 226, 111198. doi:10.1016/j.compstruct.2019.111198

Yu, J., Wu, H. L., and Leung, C. K. (2020). Feasibility of using ultrahigh-volume limestone-calcined clay blend to develop sustainable medium-strength Engineered Cementitious Composites (ECC). *J. Clean. Prod.* 262, 121343. doi:10.1016/j.jclepro.2020.121343

Yu, J., Zhu, W. J., Ding, Y., Lu, Z. D., Yu, J. T., and Xiao, J. Z. (2019a). Micro-structural and mechanical properties of ultra-high performance engineered cementitious composites (UHP-ECC) incorporation of recycled fine powder (RFP). *Cem. Concr. Res.* 124, 105813. doi:10.1016/j.cemconres.2019.105813

Zhu, J. X., Xu, L. Y., Huang, B. T., Weng, K. F., and Dai, J. G. (2022). Recent developments in Engineered/Strain-Hardening Cementitious Composites (ECC/SHCC) with high and ultra-high strength. *Constr. Build. Mater.* 342, 127956. doi:10.1016/j.conbuildmat.2022.127956